Metallic interconnects for solid oxide fuel cell: Effect of water vapour on oxidation resistance of differently coated alloys

Sébastien Fontana *, Sébastien Chevalier, Gilles Caboche

Institut Carnot de Bourgogne, UMR 5209 CNRS – Université de Bourgogne, 9 Avenue Alain Savary, BP 47870, F-21078 Dijon Cedex, France

ARTICLE INFO

ABSTRACT

The need of interconnect to separate fuel and oxidant gasses and connect individual cells into electrical series in a SOFC stack appears as one of the most important point in fuel cell technology. Due to their high electrical and thermal conductivities, thermal expansion compatibility with the other cell components and low cost, ferritic stainless steels (FSS) are now considered to be among the most promising candidate materials as interconnects in SOFC stacks. Despite the formation at 800 °C of a protective chromia Cr_2O_3 scale, it can transform in volatile chromium species, leading to the lost of its protectiveness and then the degradation of the fuel cell. A previous study demonstrated that in air, the application by metal organic chemical vapour deposition (MOCVD) of a nanometric layer of reactive element oxides (La_2O_3, Y_2O_3, Nd_2O_3) on FSS improved both the electrical conductivity and the oxidation resistance. The beneficial effect of this type of coating on FSS on oxidation resistance in H_2/H_2O (anode side) is not yet completely understood. So, the goal of this study is to apply reactive element oxide coating (La_2O_3, Y_2O_3, Nd_2O_3) on two FSS (a commercial, Crofer22APU, and a model, Fe30Cr) and to perform oxidation tests in $H_2/10\%H_2O$. Kinetics was registered for 100 h at 800 °C and the corrosion products were characterized by SEM, EDX, TEM, SIMS and XRD.

© 2008 Elsevier B.V. All rights reserved.

1. Introduction

One of the main challenges for these next 50 years is the development of electric power sources which have a negligible environmental impact. A large number of possible solutions have been proposed. Solid oxide fuel cells (SOFCs) which are solid state energy conversion devices that produce electricity by electrochemically combining fuel and air across an ionic conducting electrolyte membrane, are favored due to their fuel flexibility, their high efficiency, their high energy density and their harmless emissions (when hydrogen from renewable sources is used as fuel). Nevertheless, this kind of fuel cell has to face an important challenge; the operating temperature is around 800–1000 °C, resulting in the need of components (cathode, anode, electrolyte) sustaining severe conditions. The need of interconnects to create a stack (having to collect the electrical energy developed by the cells) and, for most part of designs, to seal every single cell (having to avoid any contact between air and hydrogen), appears as a crucial point. The main important criteria required for interconnect is an excellent electrical conductivity with an area specific resistance (ASR) below 0.1 Ω cm², an excellent oxidation resistance in air and in H_2/H_2O for 40,000 h (service lifetime) at high temperature and a thermal expansion coefficient (TEC) around 10.5×10^{-6} K^{-1} [1–3]. Moreover, the interconnects must exhibit chemical and physical compatibility and stability with adjoining electrodes and seals.

Few years ago, ceramic interconnect (such as $La_{1-x}Ca_xCrO_3$) seemed to be the best solution, but this material increased dramatically the price of the stacks and it had also low electrical conductivity [4]. Advances in the development of electrolyte–electrode material [5,6] working at lower temperature (600–800 °C) enable the use of metallic interconnects which have higher electrical and thermal conductivities, easier shaping and lower cost compared to ceramics [4,7]. If one considers resistance to high temperature corrosion as the most important interconnector property, alumina-forming alloys and silica-forming alloys would be selected [8]. The excellent protective properties of alumina and silica surface scales are, however, accompanied by an extremely low electronic conductivity. Due to the relatively high electrical conductivity of Cr_2O_3, as compared to Al_2O_3 and SiO_2 (Table 1), only chromia-forming alloys have been studied [1,7,9]. Several chromia-forming alloys have been investigated, including nickel-based, chromium-based and iron-based alloys.

Ferritic stainless steels (Crofer22APU, AL453) seem to be the best option for SOFC interconnects [7,9]. Theses materials expand correctly (Table 1), they show a quite good electrical resistivity and they are highly shapeable.

* Corresponding author. Tel.: +33 3 80 39 61 58; fax: +33 3 80 39 61 32.
  E-mail address: sebastien.fontana@u-bourgogne.fr (S. Fontana).

Table 1
Material properties [1].

Materials	Thermal expansion coefficient (25–1000 °C) (10^{-6} °C^{-1})	Electrical resistivity (Ω cm)
Al_2O_3	8	5×10^8 at 700 °C
Cr_2O_3	9.6	10^2 at 800 °C
NiO	14	5–7 at 900 °C
YSZ	10.5	19
Ni-YSZ	11–12	–
$LaCrO_3$	9.5	2.9 at 1000 °C
Crofer 22 APU	12.2	5×10^{-5}
La_2O_3	–	10^7 at 600 °C
Nd_2O_3	–	10^8 at 800 °C
Y_2O_3	–	10^{11} at 800 °C
$LaMnO_3$	–	10^{-2} at 1000 °C
TiO_2	–	10^2 at 900 °C
$Cr_{1.5}Mn_{1.5}O_4$	7.5	20

At high temperature, an electrically conductive chromia (Cr_2O_3)-based thermally grown oxide (TGO) layer forms and grows on surface alloys. Unfortunately, the continued growth of the TGO scale introduces deleterious phenomenon. First, chromia scales exhibit poor electrical conductivity [7,9,10], which may increase the power loss at the cathode/interconnect and at the anode/interconnect interface during long-term operation. Some studies [9,11] revealed that, in most cases, outward chromium transport is the dominant growth process in the chromia scales whereas the contribution of oxygen transport is substantially smaller. Outward chromium diffusion results in the formation of voids and cavities at the scale/metal interface leading to poor scale adherence [12]. Thus, after exposure over thousand hours, the chromia layer can exhibit localized spallation. Finally, the last problem has been identified to be the formation of volatile gaseous Cr (VI) species such as CrO_3 or $CrO_2(OH)_2$ [13–16]. Therefore, the volatile chromium species can cause serious cell performance degradation, due to poisoning.

Several solutions have been proposed to improve the behavior of chromia-forming alloys used as metallic interconnect. The presence of other chemical elements in the alloys could improve the performance of the oxide layer. For example, Crofer22APU, which is FeCrMn(La/Ti) ferritic steels has been developed to be used as construction materials for SOFC interconnect [9]. Mn was added to obtain external spinel formation which is expected to decrease the formation of volatile Cr-species and to enhance the electrical conductivity of the scale [7,9,14,17–19]. Ti tends to form oxide precipitates of TiO_2 at the oxide–alloy interface which improve the mechanical properties of the oxide scale and the scale adherence [9]. Reactive elements (RE: La, Nd, Y, etc.) can also improve the adhesion of the chromia scale. These RE can decrease the corrosion rate by changing the diffusion mechanism form outward diffusion of chromium to inward diffusion of oxygen [9,12,20,21]. The enhancement of the electrical properties by addition of reactive element was also observed [22–26].

Several other solutions have been proposed, specially the addition of a protective oxide layer [27,28]. Examples of common coating include: perovskites with similar compositions to SOFC cathode and previous interconnect (e.g. $La_{1-x}Sr_xMnO_3$, doped-$LaCrO_3$) [20,29–31], and spinels with different mixture of cations (e.g. $(Co,Mn)_3O_4$ or $(Cu,Mn)_3O_4$) [32–34]. These coatings vary in thickness from submicron to over 20 μm and are applied using different techniques (PVD, sol–gel, screen-printing, etc.). In a previous work Fontana et al. [24] showed that the addition of a nanometric reactive element oxide (La_2O_3, Nd_2O_3 and Y_2O_3) layer applied by metal organic chemical vapour deposition (MOCVD) on Crofer22APU, AL453 and Haynes230 improved both corrosion rate and electrical properties in air. This work and numerous works have been conducted in cathode gas environment. However, the under-

standing of the oxidation behavior in anode environment (H_2/H_2O) is very important and it is still lacking.

The literature data dealing with the effect of water vapour on chromia-forming alloys show that water vapour plays a huge role on the corrosion phenomenon. The water vapour seems to be either beneficial or detrimental. Concerning the corrosion rate, some papers are contradictory [7,35]. Brylewski et al. [29] reported similar values of k_p for oxidation of SUS430 in air and in 94%H_2/6%H_2O but the electrical resistance was higher in the anode gas than in the cathode gas. In one hand, Quadakkers et al. [36] reported the chromia scales formed on ferritic stainless steels in simulated anode gas at 800 °C were thinner than those formed in air. In the other hand, although the oxygen partial pressure is lower on the anode side, Quadakkers et al. [9] found also the oxidation rate of Cr-based ODS alloys at 950–1050 °C in a H_2/H_2O mixture (equilibrium oxygen partial pressure approximately 10^{-15} bar) was higher than in high p_{O_2} environments (Air, Ar/O_2). England and Virkar [37] oxidized Ni-based alloys (Haynes230) in H_2/H_2O and in air between 700 and 1100 °C. The growth rate of the chromia scales at 800 °C in H_2/H_2O was higher than that observed in air; moreover, the electrical resistance of the scales was higher in H_2/H_2O than in the air. Liu [38] found also that in a reducing atmosphere of Ar + 5 vol.% H_2 + 3 vol.% H_2O the electrical properties of the oxide scale is worse. Due to the technical difficulty to measure electrical resistance in H_2/H_2O, the electrical properties of the thermally grown oxide in H_2/H_2O are not well understood. One beneficial effect of water is that it can improve the adherence of the scale [39,40], especially during thermal cycling, by reducing the amount of porosity at the alloy-scale interface. The severe buckling of the scale formed on non-RE-doped chromia-forming alloys observed by many authors during air oxidation does not occur during oxidation in H_2/H_2O. For example oxide scales formed on chromia-forming alloys in H_2/H_2O showed good adhesion during cyclic oxidation at 950 °C, whereas scales formed in air in the same conditions showed spallation [9]. Conversely, on the outer part of the scale, water vapour was shown to promote the formation of less protective microporous scales [9,41].

In this study, isothermal oxidation experiments were performed at 800 °C for 100 h in $H_2/10\%H_2O$ on uncoated and La_2O_3, Nd_2O_3 and Y_2O_3-coated (by MOCVD) metallic alloys (Crofer22APU, Fe30Cr) in order to well understand the effect of water vapour on corrosion behavior. Corrosion products were carefully analyzed by scanning electron microscopy (SEM), X-ray diffraction (XRD) and secondary ions mass spectrometry (SIMS).

2. Experimental

2.1. Sample preparation

The material selected for this study was the Crofer22APU alloy provided by ThyssenKrupp VDM. In order to understand better the effect of water vapour and the effect of reactive element oxide on corrosion behavior, a Fe–Cr model system, Fe30Cr alloy, was also tested. The nominal compositions of the two alloys are given in Table 2.

Prior to oxidation or deposition, the samples of Crofer22APU were cut in squares of 1 cm × 1 cm $x \sim$ 2-mm thick, and the samples of Fe30Cr were cut in discs of 1-cm diameter $x \sim$ 2-mm thick. The surface of the specimens was abraded with silicon carbide papers of increasing fineness (from 240 up to 1200-grit) and, finally, polished with a 1 μm diamond paste followed by ultrasonic cleaning in ethanol and drying.

The reactive elements (La, Nd and Y) were introduced onto the polished sample surface as thin oxide films prepared by metal organic chemical vapour deposition (MOCVD) technique. β-Diketonate compounds were used as precursors. The details process of deposition was described elsewhere [24,42,43]. This technique

Table 2
Alloy composition in weight (%).

Wt.%	Al	C	Cr	Fe	Mn	P	S	Ti	RE
Crofer 22 APU	0.1	0.005	22	Bal	0.5	0.016	0.002	0.08	0.06 (La)
Fe30Cr	–	0.0021	29.95	Bal	–	–	0.0009	–	–

enables to form thin nanostructured oxide films of about 200 nm. The quality and composition of the coatings were systematically verified by SEM/EDX analyses on both faces of the covered sample prior to the oxidation tests.

2.2. Oxidation tests

In order to get the influence of water vapour on corrosion behavior, uncoated and coated samples were oxidized in controlled $H_2/10\%H_2O$ gas mixture under 150 mbar at 800 °C for 100 h. For evident reasons of safety, thermogravimetric analyses were performed in static mode. Fig. 1 shows a sketch of the experimental configuration. It is composed of:

- A Setaram MTB10-8 microbalance which records gravimetric data during experiments.
- Two quartz reactors heated by a symmetric furnace.
- A primary vacuum system.
- A water bath which controls the partial pressure of water vapour. In this study, the temperature of the water bath was fixed at 13 °C. This temperature imposed the partial water vapour pressure to 15 mbar according to the thermodynamic.

The sample was suspended on a quartz hook inside a quartz reactor. To start an experiment, the reactor was successively evacuated and back-filled with hydrogen three times. Then, after a last pumping, the pure water vapour was introduced. Finally hydrogen was injected in order to have a total pressure of 150 mbar with 10% of water vapour. The heating and cooling rate was 200 °C h^{-1}. The head of balance was heated and maintained at 37 °C to prevent condensation of water vapour. Equilibrium oxygen partial pressure was calculated from the thermodynamics of the reaction (1):

$$H_2O_{(g)} \Leftrightarrow H_{2(g)} + \tfrac{1}{2}O_{2(g)} \tag{1}$$

In this case, the gas mixture was equivalent at 800 °C to $p_{O_2} = 5.77 \times 10^{-16}$ Pa. If the parabolic rate law was verified, the parabolic rate constants (k_p) were derived from the measured weight change data using the commonly applied procedure from Δm versus $t^{1/2}$ plots [44].

2.3. Oxide scale analyses

The oxide surface morphologies were analyzed using a "JEOL JSM-6400F" scanning electron microscope (SEM) equipped with a field emission gun (FEG). This equipment, coupled with an energy dispersive X-ray (EDX) spectrometer was used to determine the morphology and the chemical composition of the corrosion products. Since the oxide scales were very thin after 100 h at 800 °C, SEM cross-sections were not realized on oxidized samples. Phase composition of the oxide scales were characterized by X-ray diffraction (XRD) using Cu Kα (λ = 0.154 nm) radiation with an incident angle of 1°.

To better understand the effect of water vapour on corrosion mechanism and to determine the elemental distribution through the oxide layer, uncoated and coated Crofer22APU after oxidation in air and in $H_2/10\%H_2O$ at 800 °C for 100 h were analyzed by secondary ions mass spectrometry (SIMS). Argon ions were used as primary source with energy of 10 keV and an intensity of 50 nA under a 45° incidence angle. The elemental-distribution was determined with a Cameca Riber spectrometer. The analyzed zone is about 250 μm × 250 μm with a 75 μm-diameter probe, in the center of the scanned area to avoid any crater-sidewall effects. These results can be used only to determine relative changes in composition rather than absolute compositions. In fact, SIMS signal intensity, measured in counts per second, depends on several factors (ionization rate, density of target, etc.) and not only on the element concentration.

3. Results

3.1. Oxidation behavior of uncoated and coated Crofer22APU

In a previous work [24], the oxidation test of uncoated and coated Crofer22APU in air at 800 °C showed that the oxidation kinetics obeyed a parabolic rate law and that the reactive element oxides decreased significantly the parabolic rate constants. Moreover for coated alloys, a transient stage of 5 h with an important mass gain was observed at the beginning of the oxidation. Kinetics of oxidation on uncoated and coated Crofer22APU for 100 h in $H_2/10\%H_2O$ under 150 mbar at 800 °C are presented in Fig. 2. This figure indicates that the oxidation process on specimens approximately obeys the parabolic rate law. The presence of reactive element oxide on the surface reduces the mass gain and the parabolic rate constant k_p. A comparison of mass gain and the parabolic rate constant obtained in air [24] and in $H_2/10\%H_2O$ is presented in Fig. 3.

The water vapour seems to decrease the corrosion resistance. In fact, the mass gain of uncoated Crofer22APU oxidized in $H_2/10\%H_2O$ is increased of 25% compare to the same specimen oxidized in the air. The reactive element oxide coating leads to a lower decrease of corrosion phenomenon in $H_2/10\%H_2O$ as compared to the observed decrease in air. For La_2O_3 and Nd_2O_3-coated alloy, the mass gain in $H_2/10\%H_2O$ is reduced of approximately 38% and is equivalent to that obtained in air, whereas the mass gain is only decreased by 20% in the case of Y_2O_3 coating. In addition, the parabolic rate constants
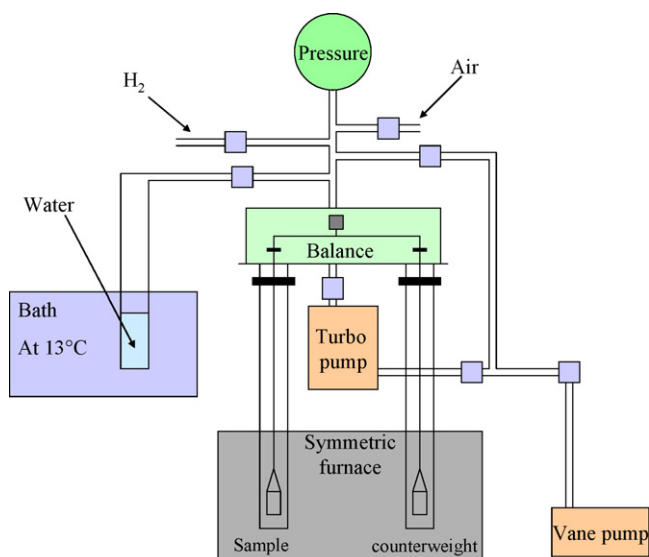
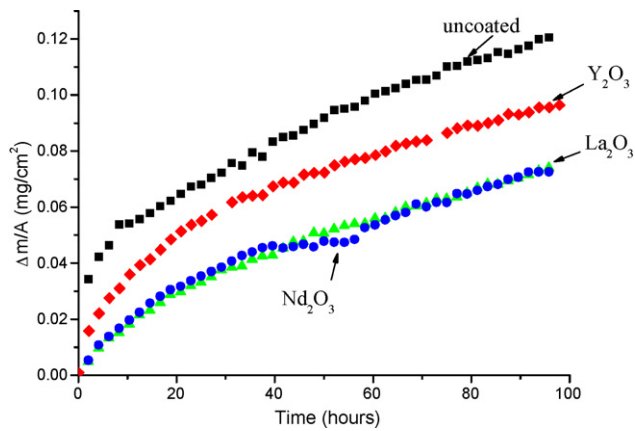**Fig. 1.** Diagram of the TGA apparatus.

Fig. 2. Kinetics (for 100 h) of coated and uncoated Crofer22APU at 800 °C in $H_2/10\%H_2O$.

of coated alloys are higher and no transient stage can be observed in $H_2/10\%H_2O$.

Fig. 4 reveals the surface morphologies of uncoated and coated samples oxidized for 100 h in $H_2/10\%H_2O$ at 800 °C. The morphology of the oxide scale is very different than that of the same sample aged in air [24]. The oxide scale on the uncoated sample (Fig. 4a) is very heterogeneous. The alloy grain boundaries are decorated by some clusters of platelets (filament shape). In the grain bulk, the oxide scale is composed of nodules enriched in Mn decorated by whiskers, covering a porous underscale of smaller grains, probably chromia according to the EDX analyses. Some traces of Ti are detected in the scale, more particularly at the alloy grain boundaries.
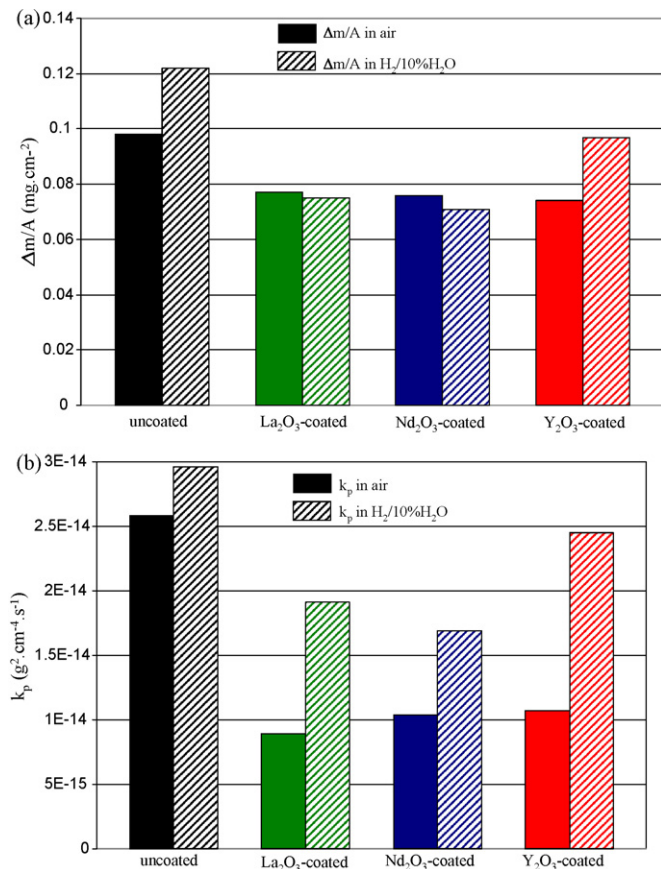

Fig. 3. Comparison of $\Delta m/A$ and k_p obtained after 100 h in air and in $H_2/10\%H_2O$ at 800 °C on Crofer22APU.

Table 3
Phases identified by XRD analyses on the surface of uncoated and coated samples of Crofer22APU in air and in $H_2/10\%H_2O$ at 800 °C.

| Atmosphere	Coating	XRD phases
Air (atmospheric pressure)	Without coating	$(Cr,Mn)_3O_4$ (major phase), Cr_2O_3
	La_2O_3 coating	$(Cr,Mn)_3O_4$ (major phase), $LaCrO_3$, Cr_2O_3 (minor phase)
	Nd_2O_3 coating	$(Cr,Mn)_3O_4$ (major phase), $NdCrO_3$, Cr_2O_3 (minor phase)
	Y_2O_3 coating	Y_2O_3 (major phase), $(Cr,Mn)_3O_4$
$H_2/10\%H_2O$ (150 mbar)	Without coating	$(Cr,Mn)_3O_4$ (major phase), Cr_2O_3, MnO (minor phase)
	La_2O_3 coating	$(Cr,Mn)_3O_4$ (major phase), Cr_2O_3, $LaMnO_3$, MnO (minor phase)
	Nd_2O_3 coating	$(Cr,Mn)_3O_4$ (major phase), Nd_2O_3, Cr_2O_3, MnO, $NdCrO_3$ (minor phase)
	Y_2O_3 coating	Y_2O_3 (major phase), $(Cr,Mn)_3O_4$, MnO, Cr_2O_3 (minor phase)

Table 3 reports the phases identified by XRD analyses on the uncoated and coated samples of Crofer22APU after oxidation in $H_2/10\%H_2O$. For comparison, XRD analyses recorded after oxidation in air were added [24]. Like in the air, after oxidation in $H_2/10\%H_2O$ of uncoated and coated Crofer22APU, chromia (ICDD card no. 38-1479) and a spinel phase $(Cr,Mn)_3O_4$ very closed to $Cr_{1.5}Mn_{1.5}O_4$ (ICDD card no. 33-0892) were detected; but in $H_2/10\%H_2O$, in addition, a few amount of MnO (ICDD card no. 75-1090) is present.

For the La_2O_3-coated sample (Fig. 4b), the oxide layers seemed to be more homogeneous than uncoated alloy, and composed of very fine grains. At the alloy grain boundaries, the oxide scale is slightly thicker and some nodules enriched in Ti and some crystallites of spinel Cr–Mn are present. XRD analyses reveal, like in air, the presence of a perovskite oxide, but it is $LaMnO_3$ (ICDD card no. 87-2012) and not $LaCrO_3$ (ICDD card no. 33-0701). The distinction between $LaMnO_3$ and $LaCrO_3$ is determined by the analyses of the intensity and d-values of the diffraction lines.

In the case of Nd_2O_3-coating, Fig. 4c shows a double-layered microstructure with a spinel oxide on the top of surface, covering a porous underscale of smaller grains enriched in Cr and Nd. Some nodules enriched in Ti are dispersed on the oxide scale surface. XRD detects the presence of Nd_2O_3 (ICDD card no. 41-1089) and some traces of $NdCrO_3$ (ICDD card no. 39-1429).

Like in air, the morphology of the Y_2O_3-coated specimen is slightly different (Fig. 4d). Typical spinel phases decorated the alloy grain boundaries and they are present at the top of the oxide scale. The deepest layer is made up of smaller grains. As in air, XRD patterns indicate the presence of yttria (ICDD card no. 41-1105) without perovskite phase.

The results of thermogravimetry and oxide scale observations show that the water vapour plays an important role on the oxidation mechanism. The distribution of chemical elements established by SIMS on uncoated and coated samples oxidized in air and in $H_2/10\%H_2O$ reveals the same phenomenon. In fact, Fig. 5a shows the elemental distribution across the oxide scale on the uncoated Crofer22APU oxidized in air. The oxide scale is around 1.9-μm thick. The surface of the oxide is enriched in Mn, Cr and O, the spinel oxide, and the underscale is only composed of Cr and O, probably chromia. The Ti signal is high at the gas–oxide interface. This could be associated with the presence of some TiO_2 particles. Furthermore, the Ti signal is also high at the metal–oxide interface. It is interesting to note that Fe concentration appears to be higher in the out part of
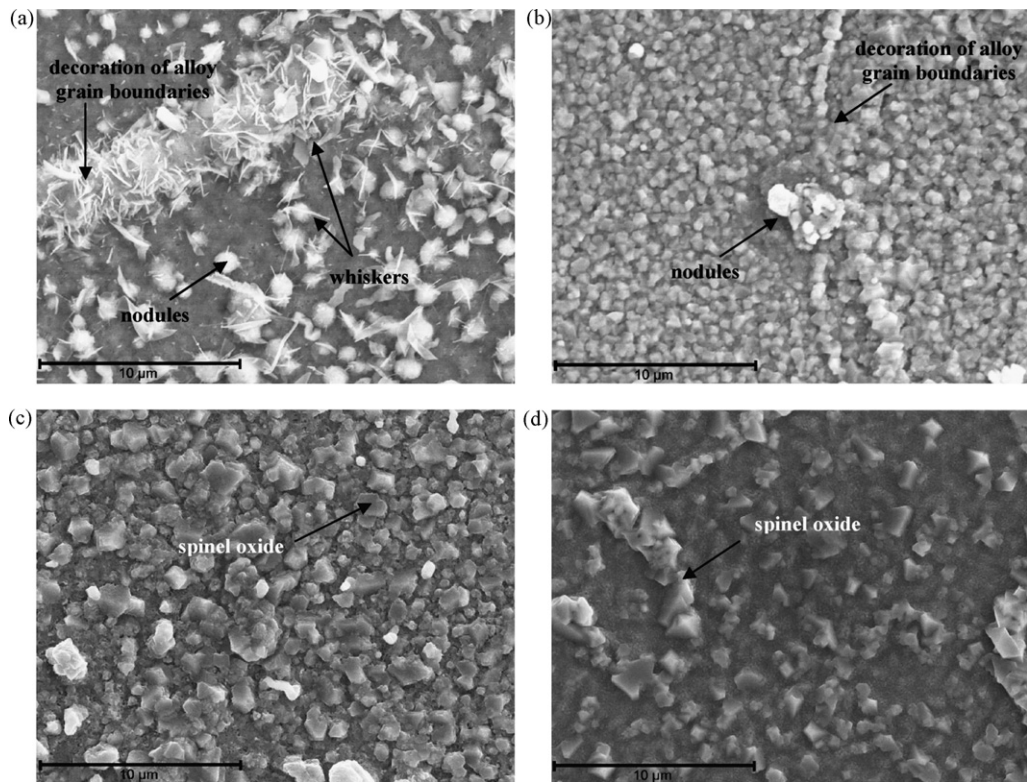
Fig. 4. SEM observations of Crofer22APU oxidized in $H_2/10\%H_2O$ at 800 °C for 100 h: (a) without coating, (b) with La_2O_3 coating, (c) with Nd_2O_3 coating and (d) with Y_2O_3 coating.

the scale than in the inner part. In the case of uncoated Crofer22APU oxidized in $H_2/10\%H_2O$ (Fig. 5b), the elemental distribution shows some differences. The oxide scale is around 1.7 µm. A scale made of chromia close to the substrate surface and a spinel phase on the oxide surface is detected. Contrary to air, Fe concentration appears to be higher in chromia scale and no more Ti signal is detected at the oxide surface.

Fig. 6a illustrates the SIMS profile of oxide scale on La_2O_3-coated Crofer22APU after oxidation in air. The oxide scale is 1.5-µm thick. La is concentrated at the interface between the forming chromia layer and the external spinel layer. This could be associated with the presence of the perovskite oxide $LaCrO_3$, identified by XRD (but doped by Ti, Fe and Mn). Even if Ti is concentrated at the metal–oxide interface, the amount of Ti and Fe is very weak at the gas–oxide interface. In the case of oxidation in $H_2/10\%H_2O$ (Fig. 6b), the elemental distribution shows that La and Mn are concentrated at the top oxide surface, probably as $LaMnO_3$ and MnO. According to this analysis, the oxide scale seems to be thicker than in air (1.7 µm). It is interesting to note that a small amount of Fe is detected at the top surface and in the chromia scale, whereas Ti is only present in the chromia scale and at the oxide–alloy interface.

In the case of Nd_2O_3-coated sample oxidized in air, the SIMS profile (Fig. 7a) is similar to that obtained for the La_2O_3-coated sample. After oxidation in air, the oxide scale is very thin, around 1 µm. The subscale is probably composed of chromia. Mn, Nd, Cr and O are concentrated at the top surface. This can be associated with the presence of $NdCrO_3$ and $(Cr,Mn)_3O_4$, identified by XRD. The signal of Ti exhibits two maxima, one at the perovskite–chromia interface and one at the oxide–alloy interface, whereas Fe presents only one maximum on the top surface. Contrary to uncoated and La_2O_3-coated alloys, the elemental distribution obtained after oxidation in $H_2/10\%H_2O$ (Fig. 7b) is closed to the elemental distribution obtained after oxidation in air. However, the oxide scale is thicker and Ti is only concentrated at the oxide–alloy interface.

The elemental distributions of the Y_2O_3-coated sample (Fig. 8) are very different. After oxidation in air, the oxide scale is 1.5-µm thick. The yttrium oxide is concentrated at the top surface of the scale and no Mn, Cr, Fe and Ti are detected in the yttria scale. The second layer is enriched in Mn and Cr, probably $(Cr,Mn)_3O_4$. Finally, the subscale seems to be chromia. Like previously, a few amount of Ti is detected at the alloy–oxide interface. The SIMS profile obtained after oxidation in $H_2/10\%H_2O$ (Fig. 8b) is slightly different. The yttria scale is also concentrated at the gas–oxide interface but a few amount of Mn is also detected, probably MnO according to the XRD measurements. A few amount of Y is also detected in the spinel scale. Ti and Fe are identified at the yttria–spinel interface. Like usual, Ti is also concentrated at the oxide–alloy interface.

3.2. Oxidation behavior of uncoated and coated Fe30Cr

Kinetics of uncoated and coated Fe30Cr oxidized at 800 °C in $H_2/10\%H_2O$ under 150 mbar for 100 h are presented in Fig. 9. All specimens follow the parabolic rate law. The presence of reactive element oxide decreases the corrosion rate. The comparison of corrosion behavior between air [45] and $H_2/10\%H_2O$ (Fig. 10) demonstrates that water vapour induces an acceleration of uncoated alloy oxidation. Its mass gain is increased of 91% compare to the same specimen oxidized in air. However, water vapour does not modify the corrosion kinetics of Y_2O_3 and Nd_2O_3-coated Fe30Cr: the mass gain is reduced of approximately 92%. The behavior of La_2O_3 seems to be quite different. Actually, even if this coating improves also the corrosion resistance in $H_2/10\%H_2O$, the mass gain and the parabolic constant obtained in $H_2/10\%H_2O$ are higher to that determined in air.

Fig. 11 shows the morphologies of samples aged 100 h in $H_2/10\%H_2O$ under 150 mbar at 800 °C. The oxide scale on the uncoated sample (Fig. 11a) is very heterogeneous. The top surface
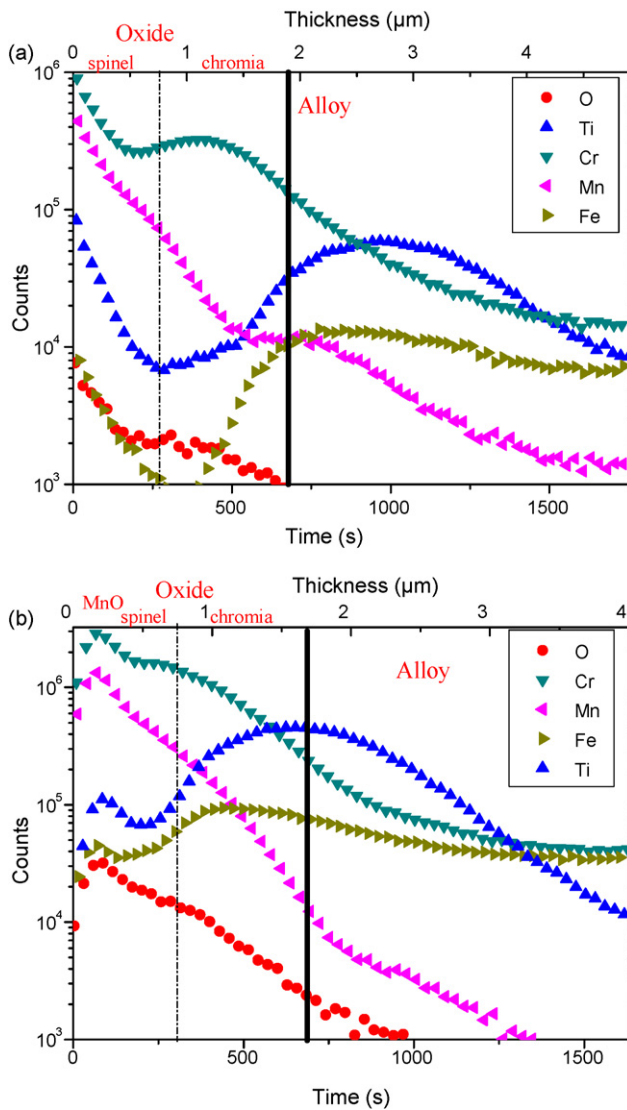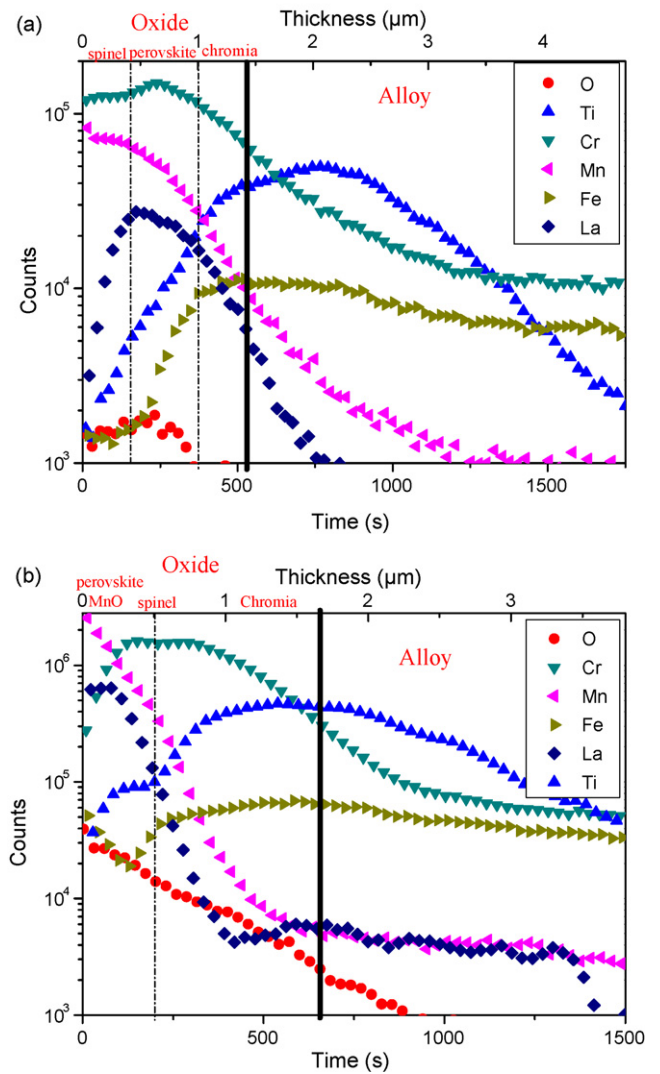
Fig. 5. SIMS profiles of oxide scale on uncoated Crofer22APU after oxidation in air (a) and in $H_2/10\%H_2O$ (b) at 800 °C for 100 h.

Fig. 6. SIMS profiles of oxide scale on La_2O_3-coated Crofer22APU after oxidation in air (a) and in $H_2/10\%H_2O$ (b) at 800 °C for 100 h.

Table 4
Phases identified by XRD analyses on the surface of uncoated and coated samples of Fe30Cr in air and in $H_2/10\%H_2O$ at 800 °C.

Atmosphere	Coating	XRD phases
Air (atmospheric pressure)	Without coating	Cr_2O_3
	La_2O_3 coating	$LaCrO_3$ (major phase), Cr_2O_3
	Nd_2O_3 coating	$NdCrO_3$ (major phase), Cr_2O_3
	Y_2O_3 coating	Y_2O_3 (minor phase), Cr_2O_3, $YCrO_3$ (minor phase)
$H_2/10\%H_2O$ (150 mbar)	Without coating	Cr_2O_3
	La_2O_3 coating	Cr_2O_3 (major phase), $La(OH)_3$, La_2O_3, $LaCrO_3$ (minor phase)
	Nd_2O_3 coating	Nd_2O_3 (major phase), Cr_2O_3
	Y_2O_3 coating	Y_2O_3 (major phase), Cr_2O_3

is covered by many needles (10 μm long), covering an underscale composed of two oxides with different geometrical shapes. The first layer is very porous and it is constituted of very fine grains. The oxide grains of the second layer have a hexagonal shape. These two types of oxide are randomly distributed on the surface. However, XRD analyses (Table 4) detected only chromia.

The oxide morphologies of the coated specimen are very different. The corrosion scale of La_2O_3-coated Fe30Cr (Fig. 11b) presents a homogeneous surface formed by spherical grains. Some pores can be also observed. XRD analyses show that the oxide is mainly composed of chromia with a few amount of perovskite $LaCrO_3$. However, additional phases are identified as La_2O_3 (ICDD card no. 22-0369) and $La(OH)_3$ (ICDD card no. 36-1481).

The oxide layer on Nd_2O_3 and Y_2O_3-coated sample (Fig. 11c–d) is a little bit different. In fact, even if the surface is homogeneous and composed of spherical grains, the scale is very porous and present some cracks randomly distributed. For Nd_2O_3-coating these cracks are much more numerous and are smaller. XRD results indicate the presence of chromia and contrary to the air show the presence of Nd_2O_3 and the absence of $NdCrO_3$. For yttria coating, the crystalline phases are chromia and especially yttria.

4. Discussion

The aim of this study was to determine the effects of water vapour on the oxidation behavior of uncoated and coated Crofer22APU and Fe30Cr. Thermogravimetric analyses demonstrated
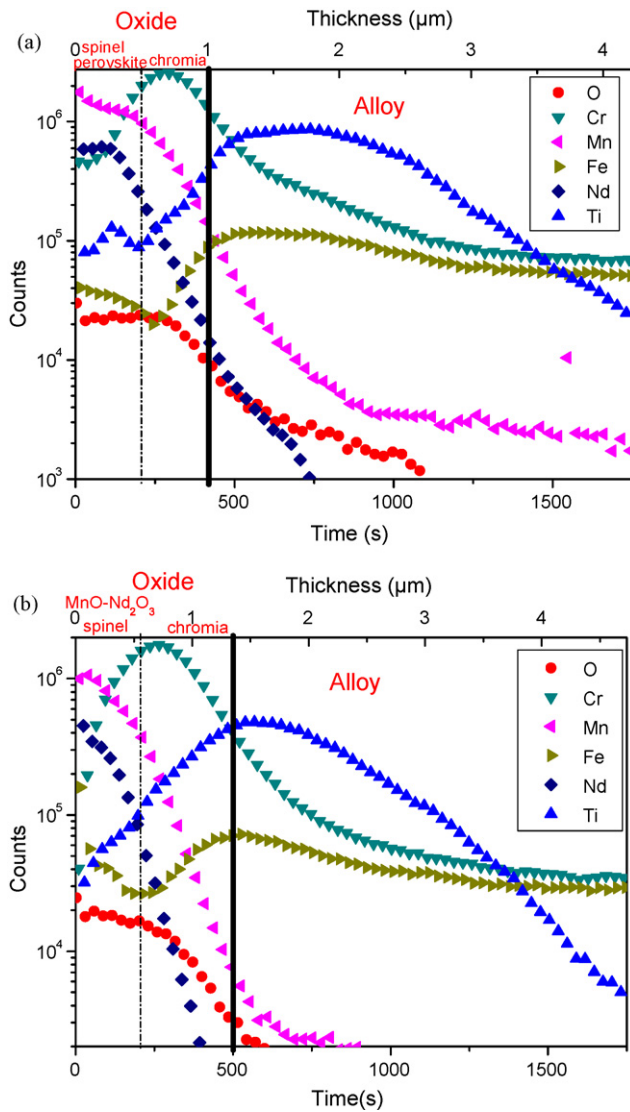
Fig. 7. SIMS profiles of oxide scale on Nd_2O_3-coated Crofer22APU after oxidation in air (a) and in $H_2/10\%H_2O$ (b) at 800 °C for 100 h.

Fig. 8. SIMS profiles of oxide scale on Y_2O_3-coated Crofer22APU after oxidation in air (a) and in $H_2/10\%H_2O$ (b) at 800 °C for 100 h.

that, like in air, the oxidation process on specimens approximately obeys the parabolic rate law. In $H_2/10\%H_2O$, there is an increase of the parabolic rate constant k_p (more particularly in the case of uncoated Fe30Cr). It can be surprising because the oxygen partial pressure is higher in air ($p_{O_2} = 2 \times 10^4$ Pa) than in $H_2/10\%H_2O$ ($p_{O_2} = 6 \times 10^{-16}$ Pa). Quadakkers et al. [9] who found the same results on Cr-based ODS alloys at 950–1050 °C in an $Ar/H_2/H_2O$-mixture, explained that the mass losses from CrO_3 evaporation are maximal in air and minimal at the low oxygen partial pressures (at low p_{O_2} $CrO_2(OH)_2$ and CrO_3 do not possess sufficient volatility to be considered [7]). This hypothesis can describe the slight increase observed in the case of Crofer22APU but cannot clarify the huge mass increase of Fe30Cr. If oxidation rates are increased, it is clear that transport of species through the oxide scale must also be increased. A main mechanism has been identified in the literature. At 800 °C in low p_{O_2}, water vapour adsorption seems to be favored [41,46]. The dissociation products of water vapour are believed to be incorporated into the oxide scale as proton or hydroxyls. The fast transport via the Grotthuss [47] proton hopping mechanism promotes inward migration of "water" (hydroxyl), but simultaneously to maintain charge neutrality, there is an increase of electronic defects and an increase of cation flux is possible. Thus the increase
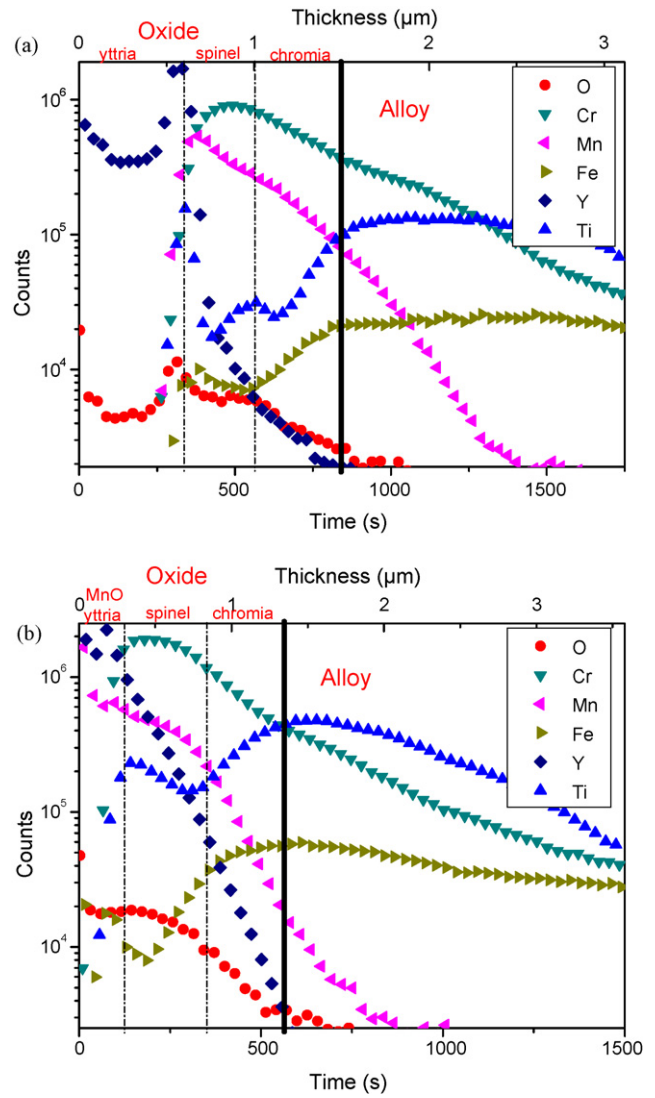
of the oxidation rate is due to the increase of the anions and cations flux.

The oxidation experiments for uncoated and coated Crofer22APU in air show important waves on the kinetics curves [24].
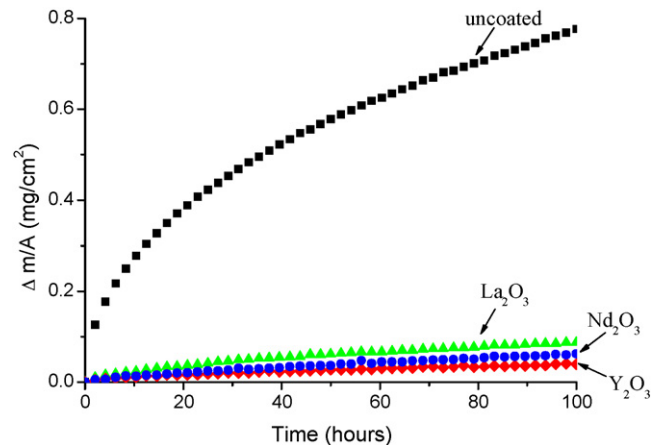

Fig. 9. Kinetics (for 100 h) of coated and uncoated Fe30Cr at 800 °C in $H_2/10\%H_2O$.
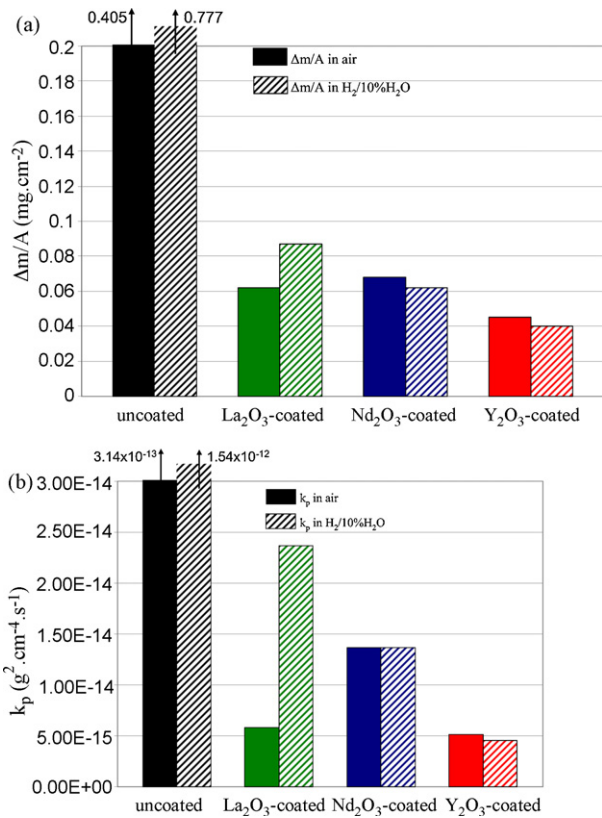
Fig. 10. Comparison of $\Delta m/A$ and k_p obtained after 100 h in air and in $H_2/10\%H_2O$ at 800 °C on Fe30Cr.

This phenomenon is due to the local cracking of the oxide scale followed by its healing [48]. The water vapour suppresses this phenomenon (because the curves obtained in $H_2/10\%H_2O$ do not present waves). The oxide scales formed on uncoated and coated alloys in wet hydrogen have a smaller grain size than when formed in the air. This fact increases the plasticity of the oxide scale and so it can enhance stress relief and prevent local cracking of the oxide scale [49].

For uncoated Crofer22APU and Fe30Cr, whiskers are frequently observed after oxidation in $H_2/10\%H_2O$, whereas flat oxide is observed after oxidation in air. Raynaud and Rapp [46] proposed a mechanism which explains the whisker formation. When p_{O_2} is very low, adsorption of H_2O becomes important and local surface catalysis of H_2O dissociation can increase locally the oxidation rate and allows the formation of platelets and whiskers ahead of the bulk scale if rapid chromium transport is possible. Furthermore, they suggest that the tips of the whisker catalyze the dissociation of H_2O. Since at high p_{O_2} oxygen adsorbs on all surface without preference, overhanging the local catalysis of water vapour, the oxide scale is so more flat without whiskers. The additions of reactive elements are known to decrease the chromium diffusion flux and thus block the formation of whiskers. This can explain why in the case of coated alloys no platelets and whiskers are observed. The decrease of the chromium diffusion is also clearly visible on the oxidation kinetics. In fact, in $H_2/10\%H_2O$, the reactive element oxide coating can decrease the parabolic rate constant. However, for Crofer22APU, the beneficial effect of reactive element oxides is less important in $H_2/10\%H_2O$ than in air.

Some pores are randomly distributed in the oxide scale on uncoated alloys. A mechanism developed by Rahmel and Tobolski [50] ("H_2/H_2O-bridges" mechanism) for scales formed by cation transport, could explain the oxide growth in moist atmospheres. If water can penetrate into the scale, oxidation of the metal surface will occur with H_2O to form new chromia and hydrogen. At
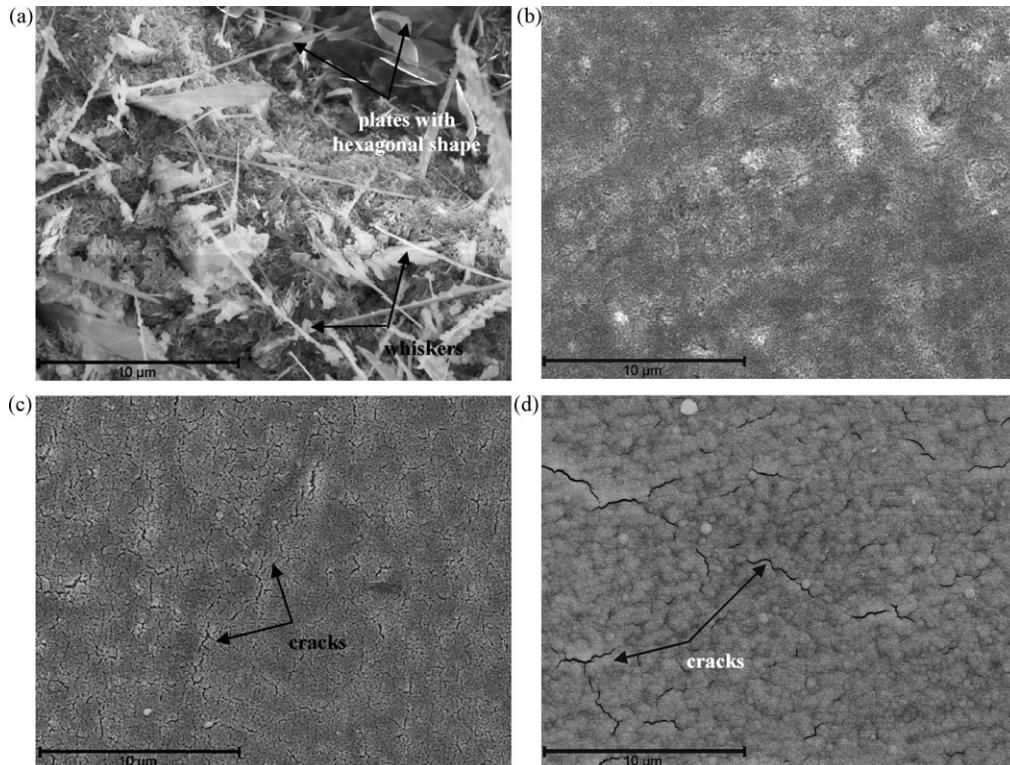

Fig. 11. SEM observations of Fe30Cr oxidized in $H_2/10\%H_2O$ at 800 °C for 100 h: (a) without coating, (b) with La_2O_3 coating, (c) with Nd_2O_3 coating and (d) with Y_2O_3 coating.

the oxide surface of the pore, the oxide is reduced by hydrogen to produce water vapour, with the net result that the pore moves outward through the scale to the oxide/gas. However, if the oxide scale is formed by oxygen ions transport in presence of reactive element, this mechanism does not explain the presence of pores in oxide scale of La_2O_3, Nd_2O_3 and Y_2O_3 coated alloys. Complementary experiments like oxidation at 800 °C in $H_2{}^{16}O/H_2{}^{18}O/D_2O$ are in progress to completely understand the effect of water vapour and reactive element on corrosion process.

The presence of water vapour seems to modify the reactivity of the reactive element oxide films on ferritic stainless steels. For La_2O_3-coated Crofer22APU and Fe30Cr oxidized in air, XRD measurements reveal that La_2O_3 coating reacts with chromia in order to form a perovskite $LaCrO_3$ (located between the spinel oxide and chromia). The elemental distribution across the oxide scales on La_2O_3-coated Crofer22APU show that the protective coating acts as a physical barrier limiting the diffusion of Fe and Ti to the surface. XRD measurements, demonstrate that the formation of the $LaCrO_3$ perovskite in $H_2/10\%H_2O$ seems to be slowed down. Actually for La_2O_3-coated Fe30Cr oxidized after 100 h at 800 °C, the initial coating is still present. These XRD results show also that water vapour can hydrolyze the La_2O_3 (presence of $La(OH)_3$) coating leading to mechanical degradation of the coating. In the case of Crofer22APU, the La_2O_3 coating reacts more preferentially with MnO in order to form a perovskite $LaMnO_3$. The SIMS profiles obtained on La_2O_3-coated Crofer22APU oxidized in $H_2/10\%H_2O$ reveals that the coating does not act as a barrier limiting the diffusion of Fe to the surface.

SIMS profiles realized on Nd_2O_3-coated Crofer22APU demonstrate that this coating does not stop the diffusion of Fe to the oxide surface (in air and in $H_2/10\%H_2O$). However, water vapour changes the reactivity of Nd_2O_3. XRD results on Fe30Cr show that the formation of $NdCrO_3$ in $H_2/10\%H_2O$ is also slowed down. However, the Nd_2O_3 coating is more resistant to water vapour, it cannot be hydrolyzed (no $Nd(OH)_3$ is detected). Furthermore, contrary to the La_2O_3 coating the Nd_2O_3 coating on Crofer22APU does not form an Nd–Mn oxide.

Generally, the yttrium oxide coating seems to have a different behavior compared to the other reactive element coatings. In air and in $H_2/10\%H_2O$, Y_2O_3 coating does not react with chromia in order to form a perovskite $YCrO_3$. This delay was already observed at higher temperature [51]. But, according to the SIMS profiles obtained on Y_2O_3-coated Crofer22APU oxidized in air, Y_2O_3 stops effectively the diffusion of Cr, Mn, Fe and Ti to the surface. The diffusion barrier is also observed after oxidation in $H_2/10\%H_2O$, whereas an increase of Mn diffusion in the yttria coating is observed in the case of the Y_2O_3-coated Crofer22APU.

The water vapour can also modify the diffusion of the alloy elements (Fe, Mn, Ti, Cr, etc.). In fact, compared to air, $H_2/10\%H_2O$ atmosphere seems to increase the concentration of Fe in the chromia scale. This phenomenon can be explained by the increase of dissolution of protons in the scale which may indirectly increase the solubility and diffusivity of iron in the chromia scale [40]. Evidence for this mechanism has been provided by dual-atmosphere experiments [18]. The water vapour enhances also the diffusion on Mn out of the oxide layer and allows the formation of MnO (already been observed by Liu [38] on Crofer22APU and Ebrite alloys).

In the same way, SIMS analyses of uncoated Crofer22APU oxidized in air show a small amount of Ti present at the oxide surface. Wouters et al. [52] established that water vapour increase the oxidation rate of titanium. In our case, after oxidation in $H_2/10\%H_2O$ Ti is also present at the metal–oxide interface but the water vapour decreases the presence of Ti at the external surface (no TiO_2 particle is detected by SEM observations). This phenomenon is surprising but has already been observed by Chandra-Ambhorn et al. [39]. It is well known that Ti is very reactive to be oxidized. This fact clearly reflects in the very low p_{O_2} of Ti/TiO ($p_{O_2} = 10^{-40}$ Pa). Thermody-

namically, this oxide should be formed in air and in $H_2/10\%H_2O$. Therefore, the reduction of Ti amount in the scale could be only explained by the decrease of Ti diffusion in presence of water vapour. Holt and Kofstad [53] demonstrated that if Ti dopes chromia by occupying the regular chromium sites in chromia (Ti^{4+}), Ti increases the electrical conductivity of chromia. They showed also that in H_2/H_2O atmosphere the hydrogen (water) solubility of Ti-doped chromia is less than in undoped chromia. Consequently in H_2/H_2O, Ti can decrease the proton defect in the oxide scale; it can then decrease the "water" diffusion and the Cr-vacancy diffusion in the chromia (in regard of the corrosion mechanism described above). This mechanism can explain partially why in the case of Fe30Cr (alloy without Ti element) the increase of corrosion rate in $H_2/10\% H_2O$ is higher than the increase of corrosion rate of Crofer22APU (alloy with a few amount of Ti).

It should be reiterated that an enhancement in the electrical conductivity and a drop in the growth rate of the oxide scale are contradicting goals; so, an acceptable compromise should be sought. It is difficult to determine the effect of water vapour on electrical properties without electrical measurements but some ideas and some comparison with the literature can be given.

In a general way, the ASR parameter measured in anode atmosphere (H_2/H_2O) is higher than in the cathode atmosphere (air) [29,37,38]. This difference between the resistances in air and in H_2/H_2O is due primarily to differences in oxide scale thickness. Because of the higher oxidation rate in H_2/H_2O – observed previously in this study – the scale is thicker, and thus has a higher electrical resistance. Moreover, it is clear that the occurrence of porosity observed on uncoated and coated alloy in the oxide scale leads to a significant increase in the electrical resistance of the oxide scale. In H_2/H_2O mixtures, Holt and Kofstadt [53] demonstrated that the conductivity could be affected by dissolved protons in the doped chromia scale and this effect depends of the doping element.

The modification of the crystalline phases in the oxide scale due to the presence of water vapour could also change the electrical conductivity of the scale. In the case of Crofer22APU aged in $H_2/10\%H_2O$, the presence of MnO which has a lower electrical conductivity than Cr–Mn spinel phase, on the oxide layer could decrease the electrical conductivity. This observation has already been observed on uncoated Crofer22APU by Liu [38]. In $H_2/10\%H_2O$, the absence of perovskite oxide likes $LaCrO_3$, $NdCrO_3$ or $YCrO_3$ (especially when these perovskites are doped by alloying elements) which have very high electrical conductivity and the presence of La_2O_3, Nd_2O_3 and Y_2O_3 which have higher electrical resistivity than that of chromia (Table 1) could increase the electrical resistivity of the oxide scale. Moreover, due to their low electrical resistance the presence of $LaMnO_3$ (Table 1) on La_2O_3-coated Crofer22APU could increase the electrical conductivity.

Current ASR tests are underway to assess the effectiveness of the surface treatments and to well understand the effect of water vapour on electrical behavior of the alloys.

This study concerned the oxidation behavior of metallic interconnect during 100 h, but the target lifetime of an interconnect is 40,000 h. Consequently, longer ageing are done in order to validate the present results. Corrosion products characterization will give crucial information about the coating performance after 1 year (8760 h), 2 years (17,520 h) and 3 years (26,280 h) at 800 °C.

5. Conclusions

High temperature oxidation tests, performed in $H_2/10\%H_2O$ on uncoated and coated Crofer22APU and Fe30Cr, showed that the water vapour has a drastic effect on the corrosion behavior and mechanism. One of the main parameters in interpreting the differences in oxidation behavior between air and wet hydrogen is that both the oxygen partial pressure and the water vapour partial

pressure are different. In anode atmospheres, the corrosion rate is higher than that in air. In $H_2/10\%H_2O$, the alloys tend to form whiskers-type oxide morphologies; the extent of whiskers formation being decreased by the addition of nanometric layer of reactive element oxide due to the reduce of outward scale growth. Another detrimental effect of water is that it can increase the porosity of the oxide scale leading to a possible increase of ASR parameter. However, water vapour can decrease the oxide scale spallation. If the water vapour increases the corrosion kinetics, the reactive element coatings (La_2O_3, Nd_2O_3 and Y_2O_3) have a beneficial effect on oxidation resistance in $H_2/10\%H_2O$ at 800 °C by reducing the Cr diffusion. Nonetheless, the reactivity of the coatings was modified by the presence of water vapour in decreasing the formation of perovskite oxide, like $LaCrO_3$, $NdCrO_3$ or $YCrO_3$. Furthermore, water vapour promotes the diffusion of Mn and Fe, promotes the formation of MnO but decreases Ti diffusion to oxide–gas interface. Finally, ASR measurements in $H_2/10\%H_2O$ will determine the effect of water vapour and the effect of reactive element on electrical behavior.

References

[1] W.Z. Zhu, S.C. Deevi, Material Research Bulletin 38 (2003) 957–972.
[2] W.Z. Zhu, S.C. Deevi, Material Sciences and Engineering A348 (2003) 227–243.
[3] V. Shemet, J. Piron-Abellan, W.J. Quadakkers, L. Singheiser, in: N. Sammes, A. Smirnova, O. Vasylyev (Eds.), Fuel Cell Technologies: State and Perspectives, Springer, Netherlands, 2005, pp. 97–106.
[4] L. Antoni, Materials Sciences Forum 461–464 (2004) 1073–1090.
[5] I. Kosacki, C.M. Rouleau, P.F. Becher, J. Bentley, D.H. Lowndes, Solid State Ionics 176 (2005) 1319–1326.
[6] F. Mauvy, J.-M. Bassat, E. Boehm, J.-P. Manaud, P. Dordor, J.-C. Grenier, Solid State Ionics 158 (2003) 17–28.
[7] J.W. Fergus, Materials Science and Engineering A397 (2005) 271–283.
[8] P. Kofstad, High Temperature Corrosion, Elsevier Applied Science, London, 1988.
[9] W.J. Quadakkers, J. Piron-Abellan, V. Shemet, L. Singheiser, Materials at High Temperatures 20 (2) (2003) 115–127.
[10] D. England, A. Virkar, Journal of Electrochemical Society 146 (1999) 3196–3202.
[11] S. Chevalier, G. Bonnet, G. Brochardt, J.C. Colson, J.P. Larpin, Materials Science Forum 369–372 (2001) 327–336.
[12] P.Y. Hou, J. Stringer, Materials Science and Engineering A202 (1995) 1–10.
[13] P. Berthod, Oxidation of Metals 64 (2005) 235–252.
[14] K. Huang, P.Y. Hou, J.B. Goodenough, Solid State Ionics 129 (2000) 237–250.
[15] B.B. Ebbinghuaus, Combustion and Flame 93 (1993) 119–137.
[16] N. Oishi, Y. Yamasaki, Electrochimical Society Proceedings 19 (1999) 759–766.
[17] G.R. Holcomb, D.E. Alman, Scripta Materialia 54 (2006) 1821–1825.
[18] Z. Yang, M.S. Walker, P. Singh, J.W. Stevenson, T. Norby, Journal of the Electrochemical Society 151 (2004) B669–B678.
[19] J.E. Hammer, S.J. Laney, R.W. Jackson, K. Coyne, F.S. Pettit, G.H. Meier, Oxidation of Metals 67 (2007) 1–38.
[20] T. Brylewski, K. Przybylski, J. Morgiel, Materials Chemistry and Physics 81 (2003) 434–437.
[21] S. Chevalier, P. Dufour, G. Bonnet, J.C. Colson, Oxidation of Metals 50 (1998) 27–49.
[22] G. Cabouro, G. Caboche, S. Chevalier, P. Piccardo, Journal of Power Sources 156 (2006) 39–44.
[23] P. Piccardo, S. Chevalier, R. Molins, M. Viviani, G. Caboche, A. Barbucci, M. Sennour, R. Amendola, Surface and Coatings Technology 201 (2006) 4471–4475.
[24] S. Fontana, R. Amendola, S. Chevalier, P. Piccardo, G. Caboche, M. Viviani, R. Molins, M. Sennour, Journal of Power Sources 171 (2007) 652–662.
[25] W. Qu, J. Li, D.G. Ivey, Journal of Power Sources 138 (2004) 162–173.
[26] D.E. Alman, P.D. Jablonski, International Journal of Hydrogen Energy 32 (2007) 2743–3753.
[27] M. Stanislowski, J. Froitzheim, L. Niewwolak, W.J. Quadakkers, K. Hilpert, T. Markus, L. Singheiser, Journal of Power Sources 164 (2007) 578–589.
[28] Z. Yang, G. Xia, G.D. Maupin, J.W. Stevenson, Surface and Coatings Technology 201 (2006) 4476–4483.
[29] T. Brylewski, M. Nanko, T. Maruyama, K. Przybylski, Solid State Ionics 143 (2001) 131–150.
[30] J.-H. Kim, R.-H. Song, S.-H. Hyum, Solid State Ionics 174 (2004) 185–191.
[31] H. Zhu, Y. Zhang, A. Basu, Z.G. Lu, M. Paranthaman, D.F. Lee, E.A. Payzant, Surface and Coatings Technology 177–178 (2004) 65–72.
[32] X. Chen, P.Y. Hou, C.P. Jacobson, S.J. Visco, L.C. De Jonghe, Solid State Ionics 175 (2005) 425–433.
[33] C. Collins, J. Lucas, T.L. Buchanan, M. Kopczyk, A. Kayani, P.E. Gannon, M.C. Deibert, R.J. Smith, D.-S. Choi, V.I. Gorokhovsky, Surface and Coatings Technology 201 (2006) 4467–4470.
[34] P.E. Gannon, C.T. Tripp, A.K. Knorpe, C.V. Ramana, M. Deibert, R.J. Smith, V.I. Gorokhovsky, V. Shutthanandan, D. Gelles, Surface and Coatings Technology 188–189 (2004) 55–61.
[35] S.R.J. Saunders, M. Monteiro, F. Rizzo, Progress in Materials Science 53 (2008) 775–837.
[36] W.J. Quadakkers, T. Malkow, J. Prion-Abellan, U. Flesch, V. Shemet, in: A.J. McEvoy (Ed.), Solid Oxide fuel Cells Forum Proceedings, vol. 2, The European Fuel Cell Forum, Switzerland, 2000, pp. 827–836.
[37] D.M. England, A.V. Virkar, Journal of the Electrochemical Society 148 (2001) A330–A338.
[38] Y. Liu, Journal of Power Sources 179 (2008) 286–291.
[39] S. Chandra-Ambhorn, Y. Wouters, L. Antoni, F. Toscan, A. Galerie, Journal of Power Sources 171 (2007) 688–695.
[40] Y. Larring, R. Haugsrud, T. Norby, Journal of Electrochemical Society 150 (2003) B374–B379.
[41] M. Hänsel, W.J. Quadakkers, D.J. Young, Oxidation of Metals 59 (2003) 285–301.
[42] C. Houngninou, S. Chevalier, J.P. Larpin, Applied Surface Science 236 (2004) 256–269.
[43] S. Chevalier, G. Bonnet, J.P. Larpin, Applied Surface Science 167 (2000) 125–133.
[44] B. Pierragi, Oxidation of Metals 27 (1987) 177–185.
[45] P. Gannon, P. Piccardo, S. Fontana, R. Amendola, S. Chevalier, G. Caboche, Journal of Applied Electrochemistry, submitted for publication.
[46] G. Raynaud, R. Rapp, Oxidation of Metals 21 (1984) 89–102.
[47] N. Agmon, Chemical Physics Letters 244 (1995) 456–462.
[48] S. Chevalier, C. Nivot, J.P. Larpin, Oxidation of Metals 61 (2004) 195–217.
[49] S. Chevalier, C. Valot, G. Bonnet, J.C. Colson, J.P. Larpin, Materials Science and Engineering A343 (2003) 257–264.
[50] A. Rahmel, J. Tobolski, Corrosion Science 5 (1965) 333–346.
[51] S. Chevalier, J.P. Larpin, Acta Materiala 50 (2002) 3105–3114.
[52] Y. Wouters, A. Galerie, J.-P. Petit, Solid State Ionics 104 (1997) 89–96.
[53] A. Holt, P. Kofstad, Solid State Ionics 117 (1999) 21–25.